Parallel and oblique firehose instability thresholds for bi-kappa distributed protons

Patrick Astfalk[1], Frank Jenko[2]

patrick.astfalk@ipp.mpg.de

[1]Max-Planck-Institut für Plasmaphysik,
Boltzmannstrasse 2, 85748 Garching,
Germany.

[2]Department of Physics and Astronomy,
University of California, Los Angeles, CA
90095, USA.

Abstract. The parallel and the oblique firehose instability are generally accepted as the leading mechanisms shaping the boundaries of the protons' pressure anisotropies observed in the solar wind for $p_{\|} > p_{\perp}$. However, it is still an open question which instability dominates this process. Only recently, first attempts were made to study the linear growth of the parallel firehose assuming more realistic bi-kappa velocity distributions instead of traditionally used bi-Maxwellians. We apply a newly developed, fully kinetic dispersion solver to numerically derive the instability thresholds for both firehose instabilities. In contrast to former findings, we observe that the presence of suprathermal populations yields a growth amplification which lowers the instability threshold of the parallel firehose. This is due to enhanced cyclotron resonance. For the first time, we also look at the oblique firehose threshold and find a contrary picture. Here, the presence of suprathermal particles leads to an increase of the instability threshold. The enhancement of the parallel firehose and the suppression of the oblique firehose are expected to be of relevance in the solar wind and may alter the competition between both instabilities. Based on our findings, we propose a method how solar wind data could be used to identify the instability mechanism dominating this competition and shaping the observed anisotropy boundary.

1. Introduction

Since *Parker* [1958] formulated a first model to explain the gross features of the solar wind, a lot of progress has been made in improving our understanding of this complex and diverse plasma system. However, many properties of the solar wind are still rather poorly understood, making this an intriguing field of ongoing research. In contrast to other astrophysical plasmas, the solar wind allows direct access by spacecraft measurements. Hence it is a good test bed to validate models which can hardly be examined in earthbound plasma experiments.

A special condition given in the solar wind, which is difficult to reproduce in experiments, is its low collisionality. The typical mean free path of solar wind particles close to the Earth orbit is of the order of 1 AU (see, e.g., *Meyer-Vernet* [2012]). The absence of collisions enables the formation and preservation of anisotropies in the pressure components parallel and perpendicular to the background magnetic field. Such anisotropies provide a source of free energy giving rise to kinetic plasma instabilities which feed on the free energy and eventually lead to a reduction of the initial pressure anisotropy.

Using Chew-Goldberger-Low theory [*Chew et al.*, 1956], it is easy to show that, assuming adiabaticity, a spherically expanding, collisionsless plasma such as the solar wind rapidly develops an excess of parallel pressure. The resulting anisotropy gives rise to the firehose instability. An unlimited growth of the anisotropy is then prevented since the firehose instability will keep the plasma close to a state of marginal stability which is determined by the firehose instability threshold. Space observations revealed that the proton pressure anisotropies encountered in the solar wind are indeed confined to a clearly constrained parameter space which is most likely shaped by the presence of kinetic instabilities[*Kasper et al.*, 2002; *Hellinger et al.*, 2006; *Bale et al.*, 2009]. In the realm $p_\parallel > p_\perp$ and $\beta_\parallel \geq 1$, the constraint is believed to be either due to the parallel propagating firehose instability ($k_\perp = 0$) or the oblique firehose instability ($k_\perp \neq 0$). Both instablities can be present simultaneously and show comparable growth rates over a wide range of parameters[*Hellinger and Matsumoto*, 2000]. This poses the question which of both instabilities is the dominant one limiting the observed pressure anisotropies. Recent investigations with hybrid expanding box simulations showed that the saturation mechanism of the parallel firehose instability might be too weak to keep an expanding plasma at marginal stability[*Hellinger and Trávníček*, 2008]. Instead, it is the saturation of the oblique firehose which ultimately prevents the pressure anisotropy from unlimited growth. However, this finding might not apply to the real solar wind since, due to numerical limitations, the simulations assumed unrealistically fast expansion. Slower expansion might favour the parallel firehose, instead[*Hellinger and Trávníček*, 2008]. This is also supported in a more recent work by *Yoon and Seough* [2014]. By combining a kinetic-fluid model of the solar wind with quasi-linear instability theory in a one-dimensional setup, *Yoon and Seough* [2014] found that the parallel firehose stops the adiabatic growth of the pressure anisotropy before it crosses the threshold of the oblique firehose instability.

Although the saturation mechanisms of both instabilities are nonlinear in nature, the corresponding linear instabilty thresholds are expected to play an important role since they determine the state of marginal stability. However, plotting numerically derived linear thresholds over the pressure anisotropies measured in the solar wind gives only rough agreement between data and theory, which is not completely satisfying neither for the parallel firehose nor for the oblique firehose (see, e.g., *Hellinger et al.* [2006]). There can be several reasons for this discrepancy. Since the expansion of the solar wind is constantly driving the firehose instability, a simple linear treatment excluding all nonlinearities arising from high magnetic field amplitudes might lack important effects. Usually, the linear approach is also combined with the assumption of homogeneity which is questionable in the presence of turbulent fluctuations[*Hellinger et al.*, 2015]. In this case, expanding box models should rather be applied in order to fully capture the nonlinear saturation of kinetic instabilities and their interplay with turbulence.

And even if exclusively linear effects determine the observed anisotropy boundaries, there are still many challenges which complicate an accurate fitting of theoretical thresholds. For further discussion on this matter, see Sec. 4.

A major limitation which narrows a realistic description of solar wind properties is the frequenctly used restriction to bi-Maxwellian particle velocity distributions of the form

$$f_\alpha = \frac{1}{\pi^{3/2}} \frac{1}{v_{\parallel\alpha}} \frac{1}{v_{\perp\alpha}^2} \exp\left(-\frac{v_\parallel^2}{v_{\parallel\alpha}^2} - \frac{v_\perp^2}{v_{\perp\alpha}^2} \right), \tag{1}$$

where $v_\parallel$ and $v_\perp$ are the particle velocities parallel and perpendicular to the background magnetic field. The thermal velocities of the particle species α are defined by $v_{\parallel\alpha} = \sqrt{2T_{\parallel\alpha}}/m_\alpha$ and $v_{\perp\alpha} = \sqrt{2T_{\perp\alpha}/m_\alpha}$ where T_α and m_α are the particles' temperature and mass. Due to the lack of collisions in the solar wind medium there is no solid fundament for this assumption, and, as is revealed by space observations, proton velocity distributions indeed exhibit non-thermal features such as beams and suprathermal particle populations following power-laws instead of Maxwellians.

For the sake of a less cumbersome theoretical treatment, solar wind data which deviates too strongly from a bi-Maxwellian model is often discarded, as is the case, e.g., for the proton anisotropy analysis presented in *Kasper et al.* [2002], *Hellinger et al.* [2006] and *Bale et al.* [2009]. Allowing departures from the bi-Maxwellian assumption increases the amount of accessible data giving further insight into the complexity of solar wind processes away from thermal equilibrium, but the theoretical analysis requires more sophisticated numerical tools.

In 1968, Olbert and Vasilyunas found that commonly observed suprathermal populations can often be fitted by kappa distributions[*Olbert*, 1968; *Vasyliunas*, 1968]. Non-thermal high-energy tails are directly measured throughout the solar wind[*Gloeckler et al.*, 1992], from the solar corona[*Ko et al.*, 1996] to the termination shock[*Decker et al.*, 2005], as well as in planetary magnetospheres[*Paschalidis et al.*, 1994; *Krimigis et al.*, 1983; *Leubner*, 1982]. For anisotropic plasmas, the kappa distribution can be written in the form

$$f_{\kappa\alpha} = \frac{1}{\pi^{3/2}} \frac{1}{\kappa^{3/2}} \frac{1}{\theta_{\parallel\alpha}\theta_{\perp\alpha}^2} \frac{\Gamma(\kappa+1)}{\Gamma(\kappa-1/2)} \left(1 + \frac{v_\parallel^2}{\kappa\theta_{\parallel\alpha}^2} + \frac{v_\perp^2}{\kappa\theta_{\perp\alpha}^2}\right)^{-(\kappa+1)} \tag{2}$$

with $3/2 \leq \kappa \leq \infty$ and with the modified thermal velocities $\theta_{\parallel\alpha} = \sqrt{\frac{2\kappa-3}{\kappa}\frac{T_{\parallel\alpha}}{m_\alpha}}$, $\theta_{\perp\alpha} = \sqrt{\frac{2\kappa-3}{\kappa}\frac{T_{\perp\alpha}}{m_\alpha}}$. $\Gamma(x)$ denotes the gamma function. For $\kappa \longrightarrow \infty$, this distribution degenerates to the bi-Maxwellian while for decreasing κ it assumes more and more distinct high-energy tails. Due to their frequent appearance in space plasmas, kappa distributions enjoy growing interest in the space plasma community[*Pierrard and Lazar*, 2010]. The origin of the observed high-energy tails is still in the focus of current research. They appear in association with high-amplitude plasma waves and turbulence[*Hasegawa et al.*, 1985; *Leubner*, 2000; *Yoon*, 2012] and, remarkably, κ-like power-law distributions can be derived as quasi-equilibrium solutions in the frame of Tsallis statistics which presents a possible generalization of Gibbs-Boltzmann statistics to systems with long-range forces[*Tsallis*, 1988; *Leubner*, 2002; *Silva et al.*, 2002].

It turned out that the presence of suprathermal tails in a plasma can significantly change the dispersion properties of kinetic instabilities (see, e.g., *Xue et al.* [1996]; *Leubner and Schupfer* [2000]; *Lazar et al.* [2011]). Even slight departures from a bi-Maxwellian can alter the instabilities' growth rates and hence the corresponding thresholds, if resonant populations are affected.

In this paper, we revisit the thresholds of the parallel and the oblique firehose instability and we demonstrate that especially for low $\beta_\parallel$ the linear thresholds in kappa-distributed plasmas show obvious deviations from bi-Maxwellian setups. We also discuss how this could be exploited to identify the instability mechanism which is responsible for the anisotropy boundary observed in the solar wind in the regime $T_\perp/T_\parallel < 1$.

For the numerical calculations, we make use of the recently published fully-kinetic dispersion relation solver DSHARK [*Astfalk et al.*, 2015] and we compare our findings to former results obtained by *Lazar et al.* [2011].

The remainder of this paper is organized as follows. First, we discuss linear kinetic theory of small-amplitude waves in bi-Maxwellian and bi-kappa plasmas. In section 3, we focus on the linear instability thresholds of the parallel and oblique firehose and we analyze the effect of suprathermal populations on their dispersion properties. And finally, in section 4, we summarize and discuss our results.

2. Linear Theory

The firehose instability was first derived in the context of kinetic magnetohydrodynamics (see, e.g., *Rosenbluth* [1956]). However, despite the traditional consideration as a fluid instability the firehose is generally of resonant character and requires a fully kinetic treatment[*Gary et al.*, 1998]. A careful inspection reveals that especially for low beta,

$\beta_\parallel \lesssim 1$, this is of paramount importance since a fluid approximation yields a dramatic underestimation of the expected growth rates.

To derive the dispersion relation of waves in a magnetized, homogeneous and collisionless plasma, the Vlasov-Maxwell system of equations is employed. Linearizing the equations and using Fourier transformations, the dielectric tensor ϵ can be derived which describes the plasma's linear response to small-amplitude perturbations. Solving the general dispersion equation for wave propagation in plasmas,

$$0 = \det\left(\frac{c^2k^2}{\omega^2}\left(\frac{\mathbf{k}\otimes\mathbf{k}}{k^2} - 1\right) + \epsilon\right), \tag{3}$$

then gives the dispersion relation $\omega(k)$. In general, this formalism can be applied to plasmas with arbitrary distribution functions. For Maxwellian plasmas, it is helpful to introduce the plasma dispersion function

$$Z(\xi) = \frac{1}{\sqrt{\pi}}\int_{-\infty}^{\infty}\frac{\exp\left(-s^2\right)}{s-\xi}ds \tag{4}$$

defined by *Fried and Conte* [1961]. The components of the dielectric tensor for a bi-Maxwellian medium can then be written as given, e.g., in *Brambilla* [1998]. Assuming bi-kappa distributed particles a modified plasma dispersion function

$$Z^*_\kappa(\xi) = \frac{1}{\sqrt{\pi}}\frac{1}{\kappa^{3/2}}\frac{\Gamma(\kappa+1)}{\Gamma(\kappa-1/2)}\int_{-\infty}^{\infty}\frac{ds}{(s-\xi)(1+s^2/\kappa)^{\kappa+1}} \tag{5}$$

was introduced by *Summers and Thorne* [1991] and expressions for the components of the corresponding dielectric tensor were derived in *Summers et al.* [1994].

For purely parallel propagating modes ($k_\perp = 0$), it is easy to show that the dispersion relation greatly simplifies to the parallel kinetic equation

$$0 = 1 - \frac{k_\parallel^2c^2}{\omega^2} + \pi\sum_\alpha\left(\frac{\omega_{\mathrm{p}\alpha}}{\omega}\right)^2\int\limits_{-\infty}^{\infty}dv_\parallel\int\limits_0^{\infty}dv_\perp v_\perp^2\frac{(\omega - k_\parallel v_\parallel)\frac{\partial f_\alpha}{\partial v_\perp} + k_\parallel v_\perp\frac{\partial f_\alpha}{\partial v_\parallel}}{\omega - k_\parallel v_\parallel \pm \Omega_\alpha}. \tag{6}$$

For a bi-Maxwellian plasma with f_α given by equation (1), this can be rewritten as

$$0 = 1 - \frac{c^2 k_\parallel^2}{\omega^2} + \sum_\alpha \frac{\omega_{p\alpha}^2}{\omega^2} \left(\frac{\beta_{\perp\alpha}}{\beta_{\parallel\alpha}} - 1 + \left(\frac{\omega}{k_\parallel v_{\parallel\alpha}} + \left(\frac{\beta_{\perp\alpha}}{\beta_{\parallel\alpha}} - 1 \right) \xi_\alpha \right) Z\left(\xi_\alpha\right) \right), \quad (7)$$

where $\xi_\alpha = \frac{\omega \mp \Omega_\alpha}{k_\parallel v_{\parallel\alpha}}$.

For a bi-kappa plasma, we get

$$0 = 1 - \frac{c^2 k_\parallel^2}{\omega^2} + \sum_\alpha \frac{\omega_{p\alpha}^2}{\omega^2} \left(\frac{\beta_{\perp\alpha}}{\beta_{\parallel\alpha}} - 1 + \left(\frac{\omega}{k_\parallel v_{\parallel\alpha}} + \left(\frac{\beta_{\perp\alpha}}{\beta_{\parallel\alpha}} - 1 \right) \xi_\alpha \right) \times \quad (8)$$

$$\frac{2\kappa-2}{2\kappa-3} \sqrt{\frac{\kappa-1}{\kappa}} Z_{\kappa-1}^* \left(\sqrt{\frac{\kappa-1}{\kappa}} \xi_\alpha \right) \right), \quad (9)$$

with $\xi_\alpha = \frac{\omega \mp \Omega_\alpha}{k_\parallel \theta_{\parallel\alpha}}$.

The lower (upper) sign in ξ_α is for right- (left-) handed circularly polarized waves. For the parallel firehose instability, right-hand polarization is considered.

3. The firehose instability

In the existing literature, the thresholds of the parallel and the oblique firehose instability are frequently discussed and compared to solar wind data (see, e.g., *Kasper et al.* [2002]; *Hellinger et al.* [2006]; *Bale et al.* [2009]). However, the analysis is mostly restricted to the core protons which are fitted by bi-Maxwellian velocity distributions. Data which deviates too strongly from the bi-Maxwellian model, e.g. due to the presence of beams or nonthermal high-energy tails, is often discarded. Using bi-kappa distributions in both data analysis and theory may enable a more complete understanding of the solar wind dynamics.

The dispersion properties of the parallel proton firehose in bi-kappa setups were investigated in *Lazar and Poedts* [2009] and *Lazar et al.* [2011]. The implications for the instability threshold were also briefly discussed. However, the threshold was only considered in the fluid approximation and an erroneous conclusion was drawn from a flawed

Taylor expansion in *Lazar et al.* [2011]. Thus a reconsideration of the parallel firehose threshold is in order. A more recent paper, *Viñas et al.* [2015], also describes the parallel firehose in bi-kappa distributed plasmas, but the discussion is restricted to anisotropic electrons, only. We want to focus on the proton firehose, instead.

To our knowledge, the oblique firehose instability has never been investigated in bi-kappa setups. The reason for this might be the increased numerical effort. However, this challenge can be overcome by using the newly developed dispersion relation solver DSHARK which is based on the findings of *Summers et al.* [1994]. In this work, we present and discuss the numerically derived thresholds for the parallel and the oblique proton firehose instability in bi-kappa distributed plasmas. Throughout the paper, the electrons are assumed to be isotropic and Maxwellian with $\beta_\mathrm{e} = 1$.

3.1. The parallel firehose instability

The parallel firehose instability shows positive growth rates for propagation angles $|\theta| \lesssim 20°$. However, the maximum growth rate is always found at $\theta = 0°$, so the dispersion relation of the dominant mode can be derived by applying the parallel kinetic equation, equation (7), for a bi-Maxwellian or, equation (9), for a bi-kappa plasma, respectively. By using the large argument expansion, $|\xi_\alpha| \gg 1$, in the plasma dispersion function,

$$Z(\xi_\alpha) = -\frac{1}{\xi_\alpha} - \frac{1}{2\xi_\alpha^3} - \frac{3}{4\xi_\alpha^5} + \mathcal{O}\left(\xi_\alpha^7\right), \tag{10}$$

and keeping all terms up to order $\mathcal{O}(\delta^3)$ in equation (7), where $\delta \sim \frac{\omega}{\Omega_\alpha} \sim \frac{k v_{\parallel\alpha}}{\Omega_\alpha}$, we recover the dispersion relation of the fluid firehose instability,

$$\gamma(k) = \frac{k_\parallel v_A}{\sqrt{2}} \sqrt{\beta_\parallel - \beta_\perp - 2}, \tag{11}$$

which can also be obtained from kinetic MHD. We see that in the fluid approximation the parallel firehose is purely growing and there is an analytic instability threshold given by

$$\beta_{\|} > \beta_{\perp} + 2. \tag{12}$$

However, equation (11) is mathematically ill-posed since $\gamma \sim k$ implies the possibility of infinite growth rates. This problem can be removed by keeping higher order terms in the expansion [*Davidson and Völk*, 1968; *Yoon*, 1995].

Solving equation (7) directly with a numerical solver gives the dispersion relation for the fully kinetic parallel firehose which is different from the purely fluid-like firehose instability in two aspects. The kinetic firehose is oscillatory, $\omega_r \neq 0$, and especially for low $\beta_{\|}$, its growth rate is significantly enhanced by anomalous cyclotron resonance which becomes important for $|\xi_\alpha| \sim 1$. For a detailed study of the resonant nature of the parallel firehose, see *Gary et al.* [1998] and *Matteini et al.* [2006]. Naturally, the growth enhancement also has an impact on the corresponding instability threshold.

In Fig. 1, we plot the fluid threshold together with numerically derived thresholds allowing for different maximum growth rates, down to $\gamma_{\max}/\Omega_{\mathrm{i}} = 10^{-13}$ (compare with Fig. 1 in *Matteini et al.* [2006]). Apparently, the cyclotron resonance destabilizes the plasma also in regions where the fluid mechanism does not drive the instability. We also note that especially for low $\beta_{\|}$, the location of the threshold crucially depends on the chosen maximum growth rate. When comparing thresholds to solar wind data, the best agreement is usually found for maximum growth rates between $\tilde{\gamma}_{\max} = 10^{-1}$ and $\tilde{\gamma}_{\max} = 10^{-3}$ [*Hellinger et al.*, 2006], where γ is normalized to the proton gyrofrequency, i.e. $\tilde{\gamma} = \gamma/\Omega_{\mathrm{i}}$. This is rather empirical and there is still a lack of a physical justfication for the relevance of these time scales (we will further comment on this in section 4).

However, for the following considerations, we will continue using $\tilde{\gamma}_{\max} = 10^{-1\ldots-3}$ as reference thresholds since these are the limits often used in the literature.

Lazar et al. [2011] came to the conclusion that a decreasing κ index leads to an increase of the parallel firehose threshold to higher pressure anisotropies. Hence, the plasma is expected to become more stable in the presence of suprathermal particle populations. This conclusion was based on the large argument expansion of the modified plasma dispersion function in the parallel kinetic equation. As we saw earlier, the fluid approximation gives a rather inaccurate model for the instability threshold of the parallel firehose for low $\beta_{\parallel}$. Furthermore, we found that *Lazar et al.* [2011] missed one term in the applied large argument expansion. Redoing the calculation with equation (9) and keeping all terms up to order $\mathcal{O}(\delta^3)$, we recover the same fluid threshold, equation (12), as for the bi-Maxwellian case. Hence, the fluid mechanism of the parallel firehose instability is not sensitive to the presence of suprathermal particles but solely depends on the overall pressure anisotropy. This result can also be obtained by looking at the force balance of a perturbed magnetic field line in an anisotropic, perfectly conducting plasma. A particle flowing along a bend in the field line will feel the centrigual force $F_C = mv_{\parallel}^2/R$ where R denotes the curvature radius of the bend. This is opposed by the force acting on the particle's magnetic moment, $F_\mu = \|\nabla(\mu \cdot \mathbf{B})\| = mv_{\perp}^2/2R$, and the magnetic tension force which we approximate as $F_B = B_0^2/4\pi R$ (see, e.g., *Treumann and Baumjohann* [1997])[1]. Hence the system becomes firehose-unstable when the centrifugal force exceeds the sum of the other two forces. We add up the contribution of all particles by integrating over the particle velocity distribution f. The instability condition then reads

$$\int d^3v \frac{mv_{\parallel}^2}{R} f > \int d^3v \frac{mv_{\perp}^2}{2R} f + \int d^3v \frac{B_0^2}{4\pi R} f. \tag{13}$$

For a bi-Maxwellian distribution, given by equation (1), we immediately recover the fluid threshold, equation (12). For a bi-kappa distribution, equation (2), we get

$$\frac{2\kappa}{2\kappa-3}\frac{m\theta_\parallel^2}{2} > \frac{2\kappa}{2\kappa-3}\frac{m\theta_\perp^2}{2} + \frac{B_0^2}{4\pi}. \tag{14}$$

Using the definitions for $\theta_\parallel$ and $\theta_\perp$ this turns into the well-known fluid threshold, equation (12).

In Fig. 2, we present the thresholds of the resonant parallel firehose for different bi-kappa setups which were derived with the fully kinetic dispersion relation solver DSHARK. For maximum growth rates $\tilde{\gamma}_{\max} = 10^{-2}$ and $\tilde{\gamma}_{\max} = 10^{-3}$, we clearly see a lowering of the threshold to smaller anisotropies which is very distinctive for $\beta_\parallel \lesssim 1$. So, instead of stabilizing the plasma, high-energy tails enhance the instability in this regime. For a maximum growth rate $\tilde{\gamma}_{\max} = 10^{-1}$, the picture is reversed. Here, the presence of high-energy tails pushes the thresholds to higher anisotropies, making the plasma more stable. For high anisotropies, the bi-Maxwellian setup obviously dominates over corresponding bi-kappa scenarios while this is vice-versa for low anisotropies. This was also found by *Lazar et al.* [2011]. For reference purposes, we fitted analytical curves of the form given in *Hellinger et al.* [2006] to the numerically derived thresholds. The corresponding fit parameters can be found in appendix A.

Since the fluid mechanism of the instability does not depend on κ, we conclude that the sensitivity of the threshold to the κ index, which we observe for low $\beta_\parallel$, is related to the cyclotron-resonant nature of the parallel firehose instability. In order to get some insight into the cyclotron resonance mechanism, we solve the parallel kinetic equation, equation (6), following the usual Landau procedure (see, e.g., *Gurnett and Bhattacharjee* [2005]). Applying a low growth rate expansion, $\gamma \ll \omega_r$, which is a reasonable approximation along the $\tilde{\gamma}_{\max} = 10^{-3}$ threshold, we can find the resonant growth rate

$$\gamma_{res} = \frac{1}{\partial \Re(D(k_\parallel, \omega))/\partial \omega} \sum_\alpha \frac{\omega_{p\alpha}^2}{\omega_r^2} \pi G_\alpha(v_\parallel) \bigg|_{v_\parallel = v_{res}}, \tag{15}$$

where

$$G_\alpha(v_\parallel) = -\frac{2\pi\omega}{k_\parallel} \int_0^\infty dv_\perp v_\perp f_\alpha - \pi \int_0^\infty dv_\perp v_\perp^2 \left(v_\parallel \frac{\partial f_\alpha}{\partial v_\perp} - v_\perp \frac{\partial f_\alpha}{\partial v_\parallel} \right). \tag{16}$$

The term in the second integral can also be written in terms of the pitch angle θ as $\left(v_\parallel \frac{\partial f_\alpha}{\partial v_\perp} - v_\perp \frac{\partial f_\alpha}{\partial v_\parallel} \right) = \frac{\partial f}{\partial \theta}$. Eqs. 15 and 16 show that in the low-growth approximation the efficiency of cyclotron resonance depends on the total number of resonant particles (first term in equation (16)) and the pitch angle anisotropy at the resonance velocity, $v_{res} = \frac{\omega + \Omega_\alpha}{k_\parallel}$ (second term in equation (16)).

We found that in low-anisotropy setups, such as the one shown in Fig. 3, the resonance velocities related to the unstable wave number range are far from the core of the velocity distribution. The resonant particles are located in the tails where kappa distributions are generally more populated than Maxwellians. The first term in equation (16), which depends on the number of resonant particles, is always negative [*Gurnett and Bhattacharjee*, 2005], hence it causes a damping of the waves. However, for low-anisotropy setups, we see an enhancement of the parallel firehose instability in the presence of suprathermal populations. We conclude that the destabilizing effect of the pitch angle anisotropy must be dominant here and even overcome the damping term.

For high-anisotropy setups, such as the one shown in Fig. 4, the resonance velocities in the unstable wave number range generally move closer to the core of the distribution. Why this leads to a dominance of the Maxwellian setup remains an open question which must be addressed in the future.

3.2. The oblique firehose instability

The oblique firehose instability was first discussed in *Yoon et al.* [1993] and *Hellinger and Matsumoto* [2000] as a kinetic instability which can occur for $T_\parallel > T_\perp$ simultaneously with the parallel firehose. However, in contrast to the parallel firehose instability, the oblique firehose is non-oscillatory and has maximum growth at strongly oblique angles. Its growth rates can be comparable to or even dominate over the parallel firehose instability.

Hellinger et al. [2006] presented the thresholds of the oblique firehose instability in a bi-Maxwellian setup. It was found that along the $\tilde{\gamma}_{\max} = 10^{-3}$ threshold, the parallel firehose linearly dominates in the low-$\beta_\parallel$ regime while for $\beta_\parallel \gtrsim 7$ the oblique firehose takes over (see also Fig. 1 in *Matteini et al.* [2006]). Along the $\tilde{\gamma}_{\max} = 10^{-2}$ threshold, the oblique firehose instability starts to dominate around $\beta_\parallel \sim 5$.

Relaxing the bi-Maxwellian assumption and allowing for bi-kappa distributed ions, we observe that - similar to the parallel firehose - the threshold of the oblique firehose instability is sensitive to the presence of high-energy tails. This is not unexpected since the oblique firehose also undergoes cyclotron resonance [*Hellinger and Trávníček*, 2008]. However, its behaviour differs from what we found for the parallel firehose. Here, the presence of suprathermal ion populations leads to a stabilization of the plasma. At least for the illustrated maximum growth rates, the threshold is always shifted to higher anisotropies, regardless of the propagation angle. Exemplary thresholds are shown in Fig. 5. For reference, we fitted analytical curves to the thresholds and present the fit parameters in appendix A.

Since a finite propagation angle with respect to the background magnetic field gives rise to more complex physics, the origin of the observed behaviour is not evident and requires a more rigorous study of the cyclotron mechanism for obliquely propagating waves. However, this is beyond of the scope of this paper.

4. Conclusion

In this paper, we investigated the thresholds of the parallel and the oblique firehose instability in plasmas with bi-kappa distributed ions. Since measurements of solar wind ion distributions often show pronounced high-energy tails, bi-kappa distributions were found to be a useful extension to traditionally used bi-Maxwellians.

In contrast to former work, *Lazar et al.* [2011], we found that the resonant parallel firehose instability is enhanced by the presence of suprathermal ion populations in low anisotropy setups with $\tilde{\gamma}_{\max} \lesssim 0.01$. We suggest that this is due to the increased pitch angle anisotropy at the corresponding resonant velocities, causing stronger cyclotron resonance. In addition, we found that the oblique firehose instability threshold is also sensitive to the presence of suprathermal particles. However, in contrast to the parallel firehose instability, the threshold is always shifted to higher anisotropies, regardless of the propagation angle. Again, this is supposed to be due to the cyclotron resonant nature of the instability. However, due to the increased complexity imposed by $k_\perp \neq 0$, the detailed nature of the resonance mechanism is not obvious and calls for further investigation.

We conclude that in plasmas with suprathermal ion populations the parallel firehose instability is enhanced while, at the same time, the plasma is stabilized with respect to the oblique firehose. The differences between the thresholds in bi-Maxwellian and bi-kappa distributed plasmas were found to be significant under typical solar wind conditions, thus this effect is supposed to be of relevance in the solar wind and may alter the competition between the parallel and the oblique firehose instability. The influence of high-energy populations is most important for low $\beta_{\parallel} \lesssim 1$. However, also for higher $\beta_{\parallel}$ it can be crucial since it extends the linear dominance of the parallel firehose instability over the oblique firehose to higher $\beta_{\parallel}$.

Even slight deviations from a bi-Maxwellian were found to lead to significant shifts of the thresholds. This adds another degree of freedom in fitting instability thresholds to the pressure anisotropy boundaries observed in the solar wind. Further ambiguity can arise, if electron anisotropies and heavy ion species are included as well (see, e.g., *Michno et al.* [2014]; *Hellinger and Trávníček* [2006]). So, as long as there is no reliable argument for a meaningful limiting maximum growth rate, which properly reflects the competition between the drive and the suppression of the firehose instabilities, we cannot hope for an accurate and physically correct description of the observed solar wind anisotropy constraints. Also, there is no argument for the assumption that the threshold is set by the same maximum growth rate over the whole range of parallel beta. This complicates the matter further.

In addition, there is still uncertainty concerning the presumed dominance of the oblique firehose instability in the solar wind. We propose that the different responses of the parallel and the oblique firehose to the presence of high-energy tails can be used to solve this outstanding problem. With a suitably large and well-resolved set of solar wind data, it should be feasible to produce proton anisotropy diagrams for different kappa indices, say one for low kappa, where there are large high-energy tails present in the measured distributions, and one for very high kappa where the observed distributions are close to bi-Maxwellian. The location of the anisotropy boundary for $T_{\perp}/T_{\parallel} < 1$ could then give a clue about the leading instability mechanism shaping the boundary in the solar wind. If the boundary lies at lower anisotropies for lower kappa indices, the parallel firehose most likely limits the anisotropies. If the boundary is moving to higher anisotropies, this would confirm the expected dominance of the oblique firehose instability.

The most promising way to make further theoretical progress on this matter, is the application of expanding box simulations. They can naturally model the competition between the parallel and the oblique firehose instability under realistic solar wind conditions. Furthermore, as was found by *Matteini et al.* [2006], they self-consistently give rise to the development of high-energy tail distributions which, as we have shown in this paper, will alter the linear growth rates and the thresholds of the firehose instabilities. We therefore hope that our findings will help to understand the outcomes of past and future expanding box simulations and complete our knowledge of anisotropy driven instabilities in the solar wind.

Acknowledgments. The research leading to the presented results has received funding from the European Research Council under the European Unions Seventh Framework Programme (FP7/2007-2013)/ERC Grant Agreement No. 277870. This work was facilitated by the Max-Planck/Princeton Center for Plasma Physics. We warmly acknowledge fruitful discussions with George Morales and thank the referees for their helpful comments and suggestions. The presented results are available from the corresponding author (patrick.astfalk@ipp.mpg.de).

Appendix A: Fitting analytical curves to the instability thresholds

Hellinger et al. [2006] suggested that firehose instability thresholds may be fitted by an analytic relation of the form

$$\frac{T_\perp}{T_\parallel} = 1 + \frac{a}{\left(\beta_\parallel - \beta_0\right)^b}. \tag{A1}$$

Find below the corresponding fit parameters (a, b, β_0) for various thresholds of the parallel and oblique firehose assuming different κ indices and propagation angles θ.

Notes

1. We assume a perfectly conducting plasma here.

References

Astfalk, P., T. Görler, and F. Jenko (2015), DSHARK: A dispersion relation solver for obliquely propagating waves in bi-kappa-distributed plasmas, *Journal of Geophysical Research: Space Physics*, pp. n/a–n/a, doi:10.1002/2015JA021507, 2015JA021507.

Bale, S. D., J. C. Kasper, G. G. Howes, E. Quataert, C. Salem, and D. Sundkvist (2009), Magnetic Fluctuation Power Near Proton Temperature Anisotropy Instability Thresholds in the Solar Wind, *Physical Review Letters*, *103*(21), 211101, doi:10.1103/PhysRevLett.103.211101.

Brambilla, M. (Ed.) (1998), *Kinetic theory of plasma waves : homogeneous plasmas.*

Chew, G. F., M. L. Goldberger, and F. E. Low (1956), The Boltzmann Equation and the One-Fluid Hydromagnetic Equations in the Absence of Particle Collisions, *Royal Society of London Proceedings Series A*, *236*, 112–118, doi:10.1098/rspa.1956.0116.

Davidson, R. C., and H. J. Völk (1968), Macroscopic Quasilinear Theory of the Garden-Hose Instability, *Physics of Fluids*, *11*, 2259–2264, doi:10.1063/1.1691810.

Decker, R. B., S. M. Krimigis, E. C. Roelof, M. E. Hill, T. P. Armstrong, G. Gloeckler, D. C. Hamilton, and L. J. Lanzerotti (2005), Voyager 1 in the Foreshock, Termination Shock, and Heliosheath, *Science*, *309*, 2020–2024, doi:10.1126/science.1117569.

Fried, B. D., and S. D. Conte (1961), *The Plasma Dispersion Function*.

Gary, S. P., H. Li, S. O'Rourke, and D. Winske (1998), Proton resonant firehose instability: Temperature anisotropy and fluctuating field constraints, *Journal of Geophysical Research*, *103*, 14,567–14,574, doi:10.1029/98JA01174.

Gloeckler, G., J. Geiss, H. Balsiger, P. Bedini, J. C. Cain, J. Fischer, L. A. Fisk, A. B. Galvin, F. Gliem, D. C. Hamilton, J. V. Hollweg, F. M. Ipavich, R. Joos, S. Livi, R. A. Lundgren, U. Mall, J. F. McKenzie, K. W. Ogilvie, F. Ottens, W. Rieck, E. O. Tums, R. von Steiger, W. Weiss, and B. Wilken (1992), The Solar Wind Ion Composition Spectrometer, *Astronomy and Astrophysics Supplement Series*, *92*, 267–289.

Gurnett, D. A., and A. Bhattacharjee (2005), *Introduction to Plasma Physics*.

Hasegawa, A., K. Mima, and M. Duong-van (1985), Plasma distribution function in a superthermal radiation field, *Physical Review Letters*, *54*, 2608–2610, doi:10.1103/PhysRevLett.54.2608.

Hellinger, P., and H. Matsumoto (2000), New kinetic instability: Oblique Alfvén fire hose, *Journal of Geophysical Research*, *105*, 10,519–10,526, doi:10.1029/1999JA000297.

Hellinger, P., and P. Trávníček (2006), Parallel and oblique proton fire hose instabilities in the presence of alpha/proton drift: Hybrid simulations, *Journal of Geophysical Research (Space Physics)*, *111*, A01107, doi:10.1029/2005JA011318.

Hellinger, P., and P. M. Trávníček (2008), Oblique proton fire hose instability in the expanding solar wind: Hybrid simulations, *Journal of Geophysical Research (Space*

Physics), *113*, A10109, doi:10.1029/2008JA013416.

Hellinger, P., P. Trávníček, J. C. Kasper, and A. J. Lazarus (2006), Solar wind proton temperature anisotropy: Linear theory and WIND/SWE observations, *Geophysical Research Letters*, *33*, L09101, doi:10.1029/2006GL025925.

Hellinger, P., L. Matteini, S. Landi, A. Verdini, L. Franci, and P. M. Trávníček (2015), Plasma Turbulence and Kinetic Instabilities at Ion Scales in the Expanding Solar Wind, *The Astrophysical Journal Letters*, *811*, L32, doi:10.1088/2041-8205/811/2/L32.

Kasper, J. C., A. J. Lazarus, and S. P. Gary (2002), Wind/SWE observations of firehose constraint on solar wind proton temperature anisotropy, *Geophysical Research Letters*, *29*, 1839, doi:10.1029/2002GL015128.

Ko, Y.-K., L. A. Fisk, G. Gloeckler, and J. Geiss (1996), Limitations on suprathermal tails of electrons in the lower solar corona, *Geophysical Research Letters*, *23*, 2785–2788, doi:10.1029/96GL02449.

Krimigis, S. M., J. F. Carbary, E. P. Keath, T. P. Armstrong, L. J. Lanzerotti, and G. Gloeckler (1983), General characteristics of hot plasma and energetic particles in the Saturnian magnetosphere - Results from the Voyager spacecraft, *Journal of Geophysical Research*, *88*, 8871–8892, doi:10.1029/JA088iA11p08871.

Lazar, M., and S. Poedts (2009), Firehose instability in space plasmas with bi-kappa distributions, *Astronomy and Astrophysics*, *494*, 311–315, doi:10.1051/0004-6361:200811109.

Lazar, M., S. Poedts, and R. Schlickeiser (2011), Proton firehose instability in bi-Kappa distributed plasmas, *Astronomy and Astrophysics*, *534*, A116, doi:10.1051/0004-6361/201116982.

Leubner, M. P. (1982), On Jupiter's whistler emission, *Journal of Geophysical Research*, *87*, 6335–6338, doi:10.1029/JA087iA08p06335.

Leubner, M. P. (2000), Wave induced suprathermal tail generation of electron velocity space distributions, *Planetary and Space Science*, *48*, 133–141, doi:10.1016/S0032-0633(99)00091-4.

Leubner, M. P. (2002), A Nonextensive Entropy Approach to Kappa-Distributions, *Astrophysics and Space Science*, *282*, 573–579, doi:10.1023/A:1020990413487.

Leubner, M. P., and N. Schupfer (2000), Mirror instability thresholds in suprathermal space plasmas, *Journal of Geophysical Research*, *105*, 27,387–27,392, doi: 10.1029/1999JA000447.

Matteini, L., S. Landi, P. Hellinger, and M. Velli (2006), Parallel proton fire hose instability in the expanding solar wind: Hybrid simulations, *Journal of Geophysical Research (Space Physics)*, *111*, A10101, doi:10.1029/2006JA011667.

Meyer-Vernet, N. (2012), *Basics of the Solar Wind*.

Michno, M. J., M. Lazar, P. H. Yoon, and R. Schlickeiser (2014), Effects of Electrons on the Solar Wind Proton Temperature Anisotropy, *The Astrophysical Journal*, *781*, 49, doi:10.1088/0004-637X/781/1/49.

Olbert, S. (1968), Summary of Experimental Results from M.I.T. Detector on IMP-1, in *Physics of the Magnetosphere*, *Astrophysics and Space Science Library*, vol. 10, edited by R. D. L. Carovillano and J. F. McClay, p. 641.

Parker, E. N. (1958), Dynamics of the Interplanetary Gas and Magnetic Fields., *Astrophysical Journal*, *128*, 664, doi:10.1086/146579.

Paschalidis, N. P., E. T. Sarris, S. M. Krimigis, R. W. McEntire, M. D. Levine, I. A. Daglis, and G. C. Anagnostopoulos (1994), Energetic ion distributions on both sides of the Earth's magnetopause, *Journal of Geophysical Research*, *99*, 8687–8703, doi: 10.1029/93JA03563.

Pierrard, V., and M. Lazar (2010), Kappa Distributions: Theory and Applications in Space Plasmas, *Solar Physics*, *267*, 153–174, doi:10.1007/s11207-010-9640-2.

Rosenbluth, M. N. (1956), Stability of the Pinch, *Los Alamos Scientific Laboratory Report*, *02030*.

Silva, R., A. R. Plastino, and J. A. S. Lima (2002), A Maxwellian Path to the q-Nonextensive Velocity Distribution Function, *eprint arXiv:cond-mat/0201503*.

Summers, D., and R. M. Thorne (1991), The modified plasma dispersion function, *Physics of Fluids B*, *3*, 1835–1847, doi:10.1063/1.859653.

Summers, D., S. Xue, and R. M. Thorne (1994), Calculation of the dielectric tensor for a generalized Lorentzian (kappa) distribution function, *Physics of Plasmas*, *1*, 2012–2025, doi:10.1063/1.870656.

Treumann, R. A., and W. Baumjohann (1997), *Advanced space plasma physics*.

Tsallis, C. (1988), Possible generalization of Boltzmann-Gibbs statistics, *Journal of Statistical Physics*, *52*, 479–487, doi:10.1007/BF01016429.

Vasyliunas, V. M. (1968), A survey of low-energy electrons in the evening sector of the magnetosphere with OGO 1 and OGO 3, *Journal of Geophysical Research*, *73*, 2839–2884, doi:10.1029/JA073i009p02839.

Viñas, A. F., P. S. Moya, R. E. Navarro, J. A. Valdivia, J. A. Araneda, and V. Muñoz (2015), Electromagnetic fluctuations of the whistler-cyclotron and firehose instabilities in a Maxwellian and Tsallis-kappa-like plasma, *Journal of Geophysical Research (Space Physics)*, *120*, 3307–3317, doi:10.1002/2014JA020554.

Xue, S., R. M. Thorne, and D. Summers (1996), Growth and damping of oblique electromagnetic ion cyclotron waves in the Earth's magnetosphere, *Journal of Geophysical Research*, *101*, 15,457–15,466, doi:10.1029/96JA01088.

Yoon, P. H. (1995), Garden-hose instability in high-beta plasmas, *Physica Scripta Volume T*, *60*, 127–135, doi:10.1088/0031-8949/1995/T60/016.

Yoon, P. H. (2012), Asymptotic equilibrium between Langmuir turbulence and suprathermal electrons in three dimensions, *Physics of Plasmas*, *19*(1), 012304, doi:10.1063/1.3676159.

Yoon, P. H., and J. Seough (2014), Proton-cyclotron and firehose instabilities in inhomogeneous plasmas, *Journal of Geophysical Research (Space Physics)*, *119*, 7108–7119, doi:10.1002/2014JA020261.

Yoon, P. H., C. S. Wu, and A. S. de Assis (1993), Effect of finite ion gyroradius on the fire-hose instability in a high beta plasma, *Physics of Fluids B*, *5*, 1971–1979, doi:10.1063/1.860785.

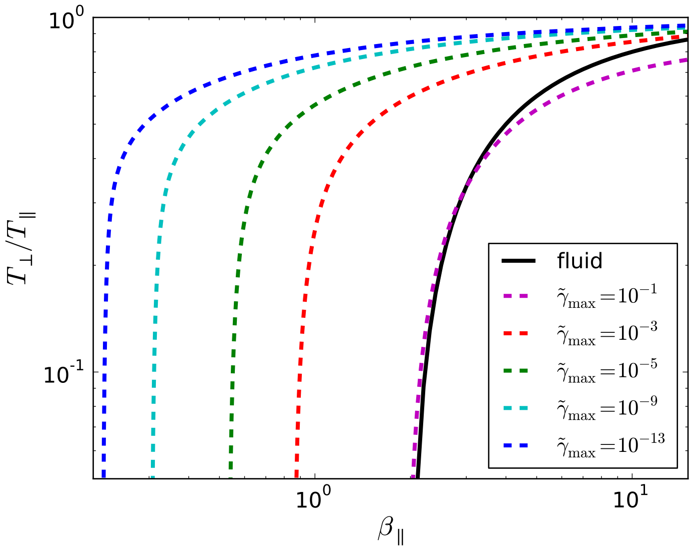

Figure 1. Instability thresholds of the resonant parallel firehose for different maximum growth rates, $\tilde{\gamma}_{\rm max} = \gamma/\Omega_{\rm i}$, compared to the fluid threshold. The electrons are isotropic and Maxwellian with $\beta_{\rm e} = 1$

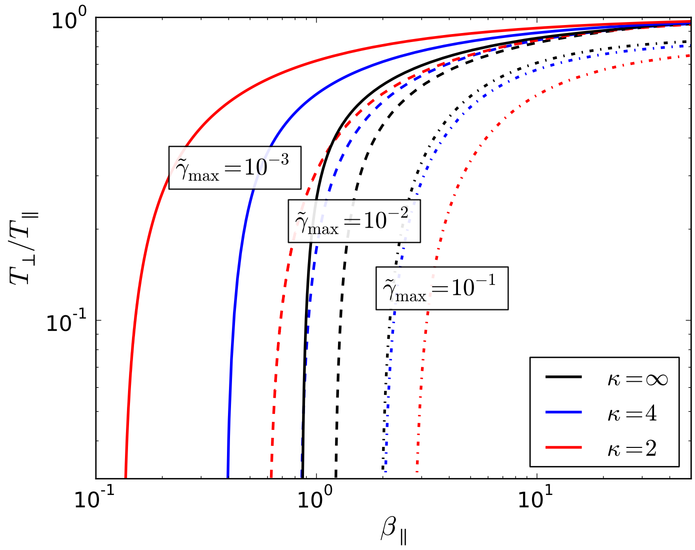

Figure 2. Instability thresholds of the resonant parallel firehose for different κ indices and maximum growth rates, $\gamma/\Omega_{\mathrm{i}} = 10^{-3}$ (solid lines), $\gamma/\Omega_{\mathrm{i}} = 10^{-2}$ (dashed lines) and $\gamma/\Omega_{\mathrm{i}} = 10^{-1}$ (dotted lines),compared to the corresponding bi-Maxwellian scenarios ($\kappa = \infty$). The electrons are isotropic and Maxwellian with $\beta_{\mathrm{e}} = 1$

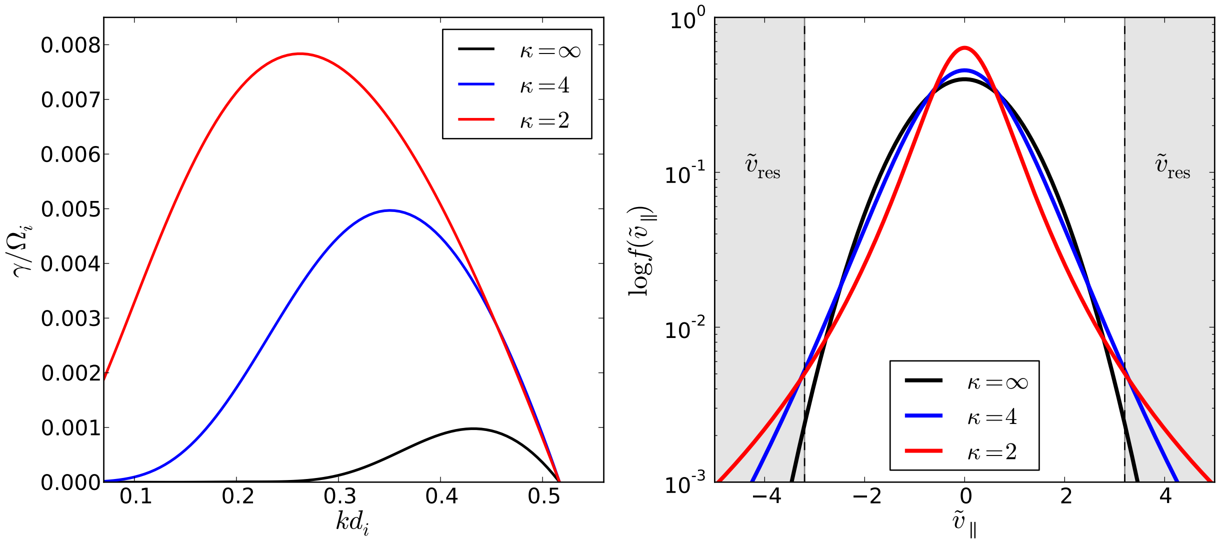

Figure 3. Growth rates of the parallel firehose instability in a low-anisotropy setup with $\beta_{\parallel\mathrm{i}} = 2.0$ and $\beta_{\perp\mathrm{i}}/\beta_{\parallel\mathrm{i}} = 0.6$ (left), and the corresponding distribution functions with highlighted resonant regimes (right). The electrons are isotropic and Maxwellian with $\beta_{\mathrm{e}} = 1$. Velocities are normalized with respect to the Alfvén velocity, $v_A = B_0/\sqrt{4\pi n_i m_i}$.

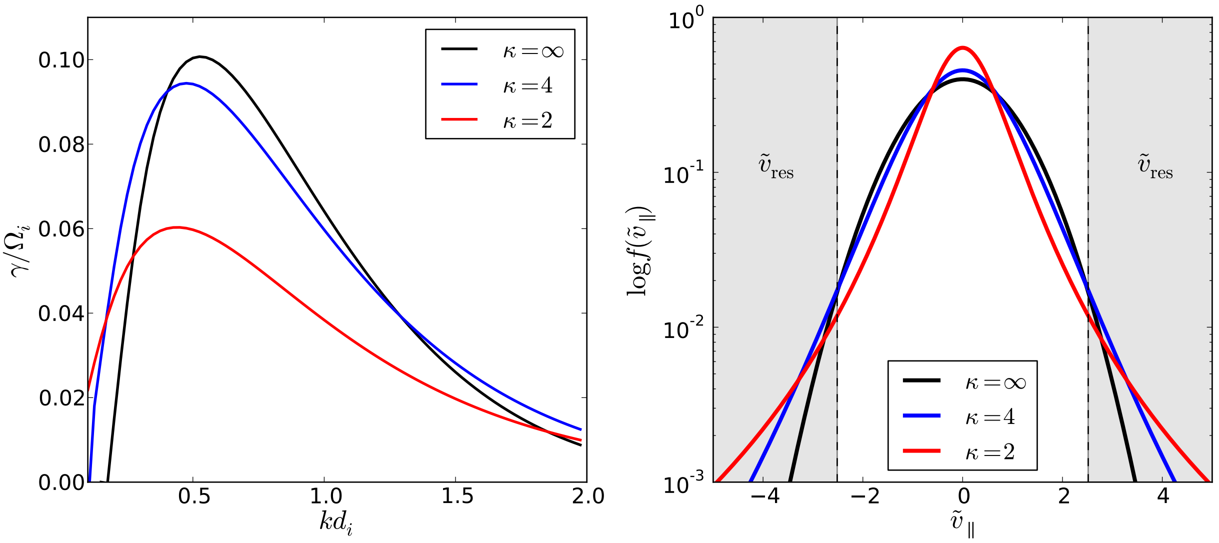

Figure 4. Growth rates of the parallel firehose instability in a high-anisotropy setup with $\beta_{\|\mathrm{i}} = 2.0$ and $\beta_{\perp \mathrm{i}}/\beta_{\|\mathrm{i}} = 0.03$ (left), and the corresponding distribution functions with highlighted resonant regimes (right). The electrons are isotropic and Maxwellian with $\beta_{\mathrm{e}} = 1$.Velocities are normalized with respect to the Alfvén velocity, $v_A = B_0/\sqrt{4\pi n_i m_i}$.

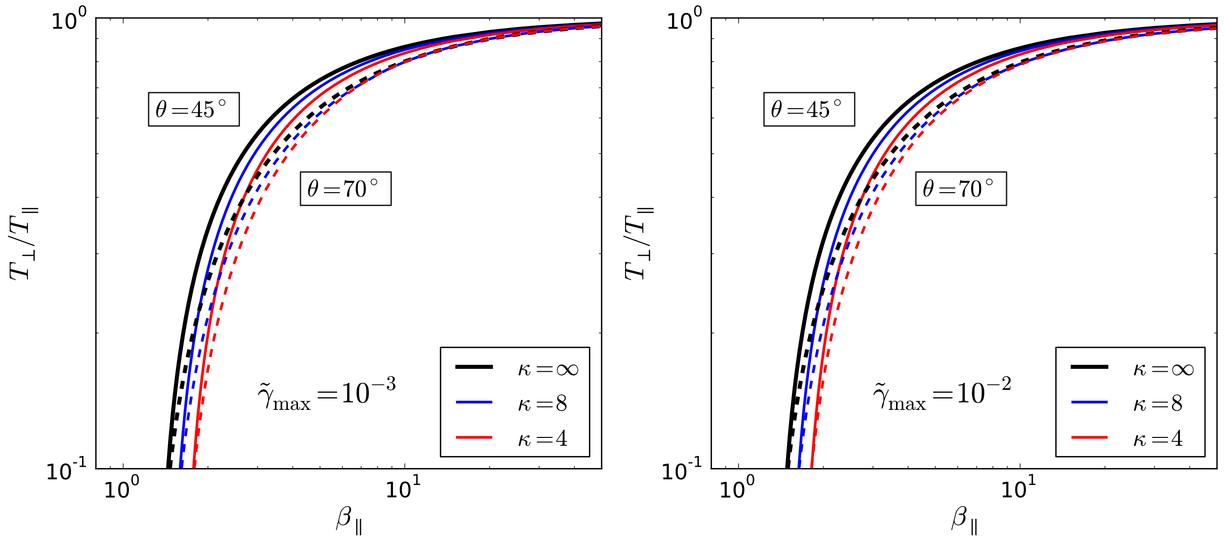

Figure 5. Thresholds of the oblique firehose instability for propagation angles $\theta = 45°$(solid lines) and $\theta = 70°$(dashed lines) for $\tilde{\gamma}_{\mathrm{max}} = 10^{-3}$ and $\tilde{\gamma}_{\mathrm{max}} = 10^{-2}$, assuming different κ indices. The electrons are isotropic and Maxwellian with $\beta_{\mathrm{e}} = 1$.

PFHI, $\theta = 0°$	a	b	β_0
Maxwell	-0.487	0.537	0.560
$\kappa = 12$	-0.438	0.475	0.503
$\kappa = 8$	-0.429	0.486	0.423
$\kappa = 6$	-0.417	0.498	0.350
$\kappa = 4$	-0.387	0.518	0.226
$\kappa = 2$	-0.274	0.536	0.042

Table 1. Fit parameters for the $\tilde{\gamma}_{\max} = 10^{-3}$ threshold of the parallel firehose instability with $\theta = 0°$, in the range $0.1 < \beta_{\|} < 50.0$.

PFHI, $\theta = 0°$	a	b	β_0
Maxwell	-0.701	0.623	0.599
$\kappa = 12$	-0.656	0.596	0.567
$\kappa = 8$	-0.623	0.579	0.569
$\kappa = 6$	-0.625	0.585	0.501
$\kappa = 4$	-0.625	0.593	0.379
$\kappa = 2$	-0.632	0.589	0.139

Table 2. Fit parameters for the $\tilde{\gamma}_{\max} = 10^{-2}$ threshold of the parallel firehose instability with $\theta = 0°$, in the range $0.1 < \beta_{\|} < 50.0$.

PFHI, $\theta = 0°$	a	b	β_0
Maxwell	-0.872	0.495	1.233
$\kappa = 12$	-0.899	0.502	1.213
$\kappa = 8$	-0.937	0.509	1.097
$\kappa = 6$	-0.947	0.505	1.088
$\kappa = 4$	-0.977	0.496	1.068
$\kappa = 2$	-1.230	0.464	1.206

Table 3. Fit parameters for the $\tilde{\gamma}_{\max} = 10^{-1}$ threshold of the parallel firehose instability with $\theta = 0°$, in the range $1.0 < \beta_\parallel < 30.0$.

OFHI, $\theta = 45°$	a	b	β_0
Maxwell	-1.371	0.996	-0.083
$\kappa = 12$	-1.444	0.995	-0.070
$\kappa = 8$	-1.484	0.994	-0.061
$\kappa = 6$	-1.525	0.993	-0.052
$\kappa = 4$	-1.613	0.990	-0.026

Table 4. Fit parameters for the $\tilde{\gamma}_{\max} = 10^{-3}$ threshold of the oblique firehose instability with $\theta = 45°$, in the range $1.0 < \beta_\parallel < 50.0$.

OFHI, $\theta = 45°$	a	b	β_0
Maxwell	-1.371	0.980	-0.049
$\kappa = 12$	-1.440	0.979	-0.034
$\kappa = 8$	-1.477	0.978	-0.024
$\kappa = 6$	-1.514	0.976	-0.012
$\kappa = 4$	-1.594	0.973	0.017

Table 5. Fit parameters for the $\tilde{\gamma}_{\max} = 10^{-2}$ threshold of the oblique firehose instability with $\theta = 45°$, in the range $1.0 < \beta_{\|} < 50.0$.